The Reliability of Curvature Estimates from Linear Elastic Tactile Sensors*

Edward J. Nicolson and Ronald S. Fearing
Department of EE&CS
University of California
Berkeley, CA 94720

Abstract

This papers analyzes the reliability of radius of curvature estimates from tactile sensor data. A linear elastic model is used to fit the indenter parameters, load, location, and curvature, to the sensor output. It was found that both contact models and calibration techniques could dramatically effect the bias and variance of the estimated indenter parameters. The Fourier series is found to be an appropriate basis in which to analyze both the calibration of tactile sensors and the problem of bandlimited shape interpretation.

1 Introduction

Recently it has been shown that the human tactile sensory system is capable of fine shape discrimination from static touch [6]. Robotic tactile sensors have also been shown to have the capability of providing curvature information [5], however results using finite-element models of tactile sensors indicate that reliable shape classification is hard [3]. It is well known that the rubber layer on the finger acts as a spatial low pass filter and that the frequency of the filter cut-off decreases as sensor depth increases [4, 11, 16], so we expect that shape sensing capabilities will depend on sensor depth. Recent theoretical results indicate that discrimination can be accomplished if the indenter class is known, however indenter classification requires shallower sensors and hence a greater sensor density than can currently be constructed in a cylindrical geometry [10].

Most robotic tactile sensors have not yet demonstrated as fine a shape discrimination ability as has been demonstrated in humans [6] despite having similar sensor densities. In many cases analysis of their performance has been limited to sensitivity of a single cell and their ability to produce "touch pictures"

to be analyzed using machine vision techniques. The main problem with using machine vision techniques is that they are not well adapted to the low resolution typically afforded by tactile sensors. Another approach is to develop tactile sensor data analysis techniques based on the mechanics of the rubber material in which they are usually embedded. In [5] it is shown how the linear elastic half space model can be used to determine contact location, curvature, orientation, and force from low resolution subsurface normal strain data on a cylindrical finger. It is the goal of this paper to extend [5] by addressing the reliability of curvature estimates. During Fearing's experiments it was found that the sensor exhibited locations of improved shape sensing capability, or "sweet spots." This paper partially explains this phenomena by comparison of model based and empirical calibration techniques.

We start by briefly reviewing the linear elastic model introduced in [11] and then use it to calibrate a tactile sensor and predict indenter parameters.

2 Linear elastic tactile sensor model

Under the assumptions of material linearity, isotropy, and homogeneity the problem of determining indenter shape, location, and total load from subsurface strain measurements on a tactile sensor may be analyzed with linear elasticity. The sensor and indenter geometry is shown in Figure 1. The cylindrical sensor has a solid core of radius r_a. An annulus of rubber is molded around the core with an outer radius of r_b. n_s sensors are evenly placed within the rubber at a radius r_s, $r_a < r_s < r_b$. An indenter of radius r_c touches the finger at location θ. The composite radius, R, which can be interpreted as the equivalent radius of the indenter if the sensor were flat, is defined as
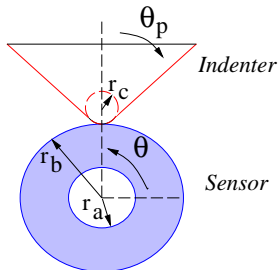
$$\frac{1}{R} = \frac{1}{r_b} + \frac{1}{r_c}.$$

Figure 1: *Sensor radii parameters and indenter shape as a function of θ_p and r_c. In the contact region the deformed profile of the sensor must match that of the rigid indenter.*
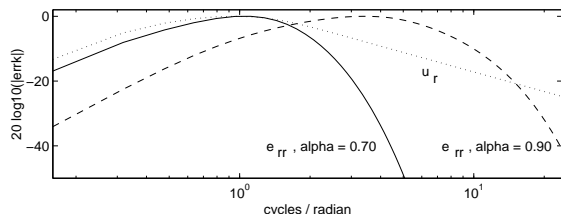

Figure 2: *Line load frequency response for normal surface displacement (dotted line) and subsurface strain at two different depths (solid and dashed lines).*

2.1 Fourier series decomposition

As we are using linear elasticity to solve this problem we may use the principle of superposition to sum independent partial solutions. Since all the partial solutions will be periodic in θ with period 2π, a Fourier series decomposition is natural. We will denote normal radial stress by τ_{rr}, radial displacement by u_r, and radial normal strain by e_{rr}. At r_b, the normal surface stress will be given by $p(\theta)$. Using a trigonometric Fourier series we can write the surface tractions as follows

$$\tau_{rr}(r_b, \theta) = p(\theta) = p_0 + \sum_{k=1}^{\infty} p_k^c \cos k\theta + \sum_{k=1}^{\infty} p_k^s \sin k\theta$$

The solution to this linear elastic problem for the boundary conditions of zero stress outside the contact region at r_b and zero displacement at r_a is given in [11].

The line-load normal-strain frequency response determines which spatial frequencies will be sensed by the tactile sensor for a given set of radii: r_a, r_s, and r_b. Figure 2 shows the strain and displacement frequency responses in a conventional Bode plot. Notice that the displacement frequency response decays very close to that of a one pole low pass filter at 20 dB/decade while the strain response decays much faster at more
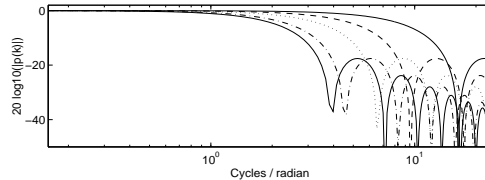

Figure 3: *Comparison of normal pressure distribution fourier coefficients for a fixed load (200 N/m) and varying $r_c \in 0.5, 1.6, 3.9, 12.3, 25.3$ mm. The largest radius has the least high frequency content.*

than 100 dB/decade. One pole low pass filters are not very good anti-aliasing filters. Thus from a filter design point of view, one would much rather use subsurface strain measurements since the strain field has a well defined frequency content whereas the frequency content of the displacement field is not clearly bandlimited.

In Figure 2 the sub-surface normal strain frequency response is shown for two different sensor depths: deep, $\alpha = r_a/r_b = 0.70$, and shallow, $\alpha = 0.90$. As deep sensors have a -40 dB cut-off at 4.5 cycles/radian and shallow sensors have their cut-off at 25 cycles/radian we expect that shallow sensors will provide better estimation of high frequency shape information.

Holding the load constant at 200 N/m, we vary the radius of the round indenter to see whether different radii indenters are distinguishable from low frequency information only. The Bode plot of the pressure distributions for 5 different indenter radii is shown in Figure 3. At 3 cycles/radian the frequency responses are clearly different and should be distinguishable with $\alpha = 0.70$ and a noise level at -40 dB.

We can investigate the r_c at which a round indenter can be distinguished from knife edge indenter by plotting the mean square error between the strain profiles at a constant load. If we assume that the sensor noise is gaussian, then the round and edge indenters can be distinguished at a 95 % level when the square root of the mean square error exceeds 2 standard deviations of the noise. Figure 4 shows the error as a function of r_c/r_b and $\alpha = r_a/r_b$. A noise plane is also shown at 2 standard deviations of the typical noise for a tactile sensor. The intersection of the noise plane with the error surface gives the boundary at which a round indenter my be distinguished from a knife edge. As would be expected, shallower sensors allow smaller radius indenters to be distinguished from a knife edge. For deep sensors with $\alpha = 0.70$, flat and edge indenters can be distinguished with noise levels as high as 3.7 % of the peak strain. If the noise is as low as 1 %
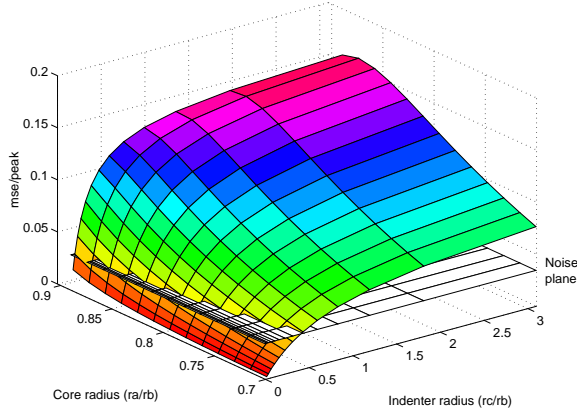
Figure 4: *Standard error as a fraction of peak strain between subsurface normal strains of knife edge and round indenters as a function of indenter radius and sensor depth.*

of peak strain then deep sensors can distinguish an indenter with $r_c/r_b = 0.16$ from an edge indenter.

2.2   The E and S maps

The shape from strain problem can be characterized by two linear maps. Letting the highest Fourier coefficient be n_c, the first map is from surface pressure Fourier coefficients, $\mathbf{p} \in \Re^{2n_c+1}$, to sampled subsurface strain, $\boldsymbol{\epsilon} \in \Re^{n_s}$. We will call this map $\mathbf{E} \in \Re^{n_s \times (2n_c+1)}$. The second is from surface pressure Fourier coefficients, $\mathbf{p}$, to indenter slope in the contact region, $\mathbf{s} \in \Re^{4n_c+2}$, for a given contact area and contact location. This map is denoted by $\mathbf{S}$. Analysis of the first map allows us to formulate sensor spacing requirements and sensing capabilities for a given depth of sensor as was done in [11]. The second map, from indenter shape to surface pressure, provides a convenient way to determine a pressure distribution for an arbitrary indenter shape. In Figure 5 the relationship between the various maps and contact models is shown with the forward directions going from left to right.

If we let

$$
\mathbf{p} = \begin{bmatrix} p_0 \\ p_1^s \\ p_1^c \\ \vdots \\ p_{n_c}^s \\ p_{n_c}^c \end{bmatrix} \quad , \quad \boldsymbol{\epsilon} = \begin{bmatrix} e_{rr}(r_s, \theta_{s_0}) \\ \vdots \\ e_{rr}(r_s, \theta_{s_{(n_s-1)}}) \end{bmatrix} \tag{1}
$$

where $\boldsymbol{\theta}_s$ is the vector of sensor locations, then the relationship between $\mathbf{p}$ and $\boldsymbol{\epsilon}$ is

$$
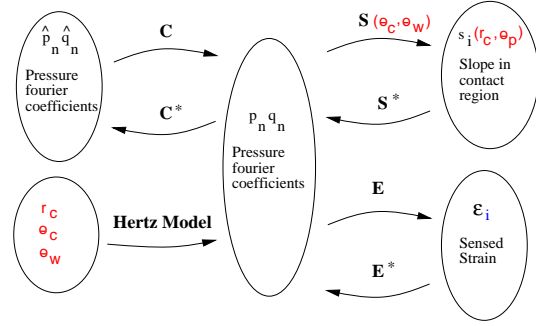\boldsymbol{\epsilon} = \mathbf{E}\mathbf{p}. \tag{2}
$$

Figure 5: *The* **S**, **C**, *and* **E** *maps. The forward, or well-conditioned, direction for each map is from left to right.*
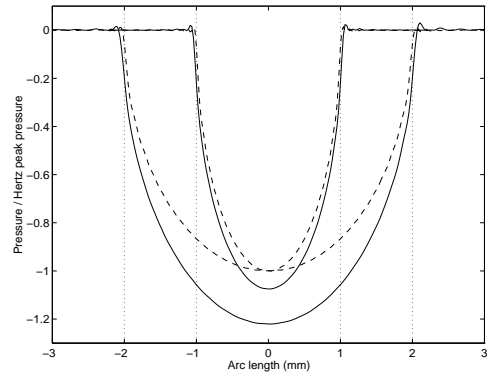

Figure 6: *Surface stress for flat frictionless indenters with 2 mm and 4 mm contact widths as given by a Hertz model (dashed lines) and a model incorporating the rigid core (solid lines). The dotted vertical lines indicate the bounds of the contact region. Both pressure distributions are divided by the peak pressure predicted by a Hertz model.*

To determine $\mathbf{p}$ from the indenter parameters radius, r_c, location, θ_c, and contact width, θ_w, one of two techniques can be used. The first is the Hertz model, described in Appendix A. The second is based on singular value decomposition and is described in [11]. In Figure 6 the normal pressure distribution predicted by each contact model is shown. As was shown by Nowell and Hillis [12], the rigid core of the cylindrical finger results in a smaller contact area than is predicted by the Hertz model for a given radius indenter, r_c, and total load, P.

3   Calibration of tactile sensors

Numerous tactile sensors have been designed and constructed [1, 7, 9, 15, 17, 18], unfortunately most of those sensors can not be used on a round finger needed for grasping and manipulation. Commercially
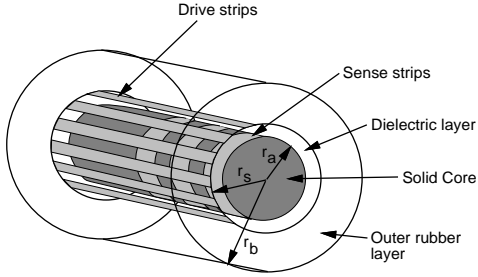
Figure 7: *Cylindrical tactile array sensor.* $r_a = 9.4$ mm, $r_s = 9.9$ mm, $r_b = 12.7$ mm, *Dielectric thickness 0.4 mm, Sensor spacing 1.52 mm.*

Joint space
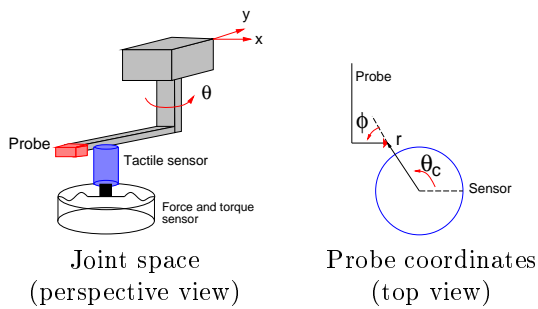(perspective view)

Probe coordinates
(top view)

Figure 8: *Prober.*

available sensors that can be used on round fingers do not provide the sensitivity required for shape discrimination. For this reason the design of [4], Figure 7, was adopted with a few changes. Sensor spacing around the circumference was halved to reduce the aliasing that was predicted by the frequency response. Dow Corning silicone rubber was used instead of isoprene rubber as silicone rubber demonstrated reduced hysteresis in preliminary experiments. A shield layer was added to reduce the proximity sensing effect that made the original design difficult to use during manipulation and wire connections were improved so that cable flexing did not affect the measured capacitance.

An accurate positioning and force measuring device, as shown in Figure 8, was required to deliver indenter touches at known locations and measure the applied contact forces. Experiments were conducted with a set of round probe tips made from machinable wax with r_c varying from 1.59 mm to 25.25 mm. In addition a 90° corner and a flat indenter were used. All indenters had a length of 4 mm and were applied so that the 4 mm length was along the axis of the sensor. This length was chosen to correspond to the dimension of the sense strip, attached to the core, along the axis of the sensor. Indenters were applied directly above the sense strip at 1° intervals with a load of 200 N/m.
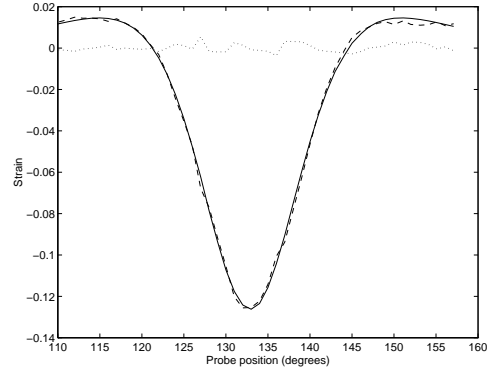

Figure 9: *Model based calibration results with an edge contact for the second sensor element . Solid line is model fit, dashed is experimental data, dotted is error.*

Both the tactile and force data were sampled 20 times at each point.

The contact force and location data were used to generate the Fourier series coefficients of the pressure distribution for each contact. If we let the total number of touches be n_t, then the Fourier coefficients for each contact may be assigned to the columns of a matrix $\mathbf{P} \in \Re^{(2n_c+1) \times n_t}$. Similarly the averaged sensor data for each touch can be assigned to the columns of the matrix $\mathbf{D} \in \Re^{n_s \times n_t}$ where n_s is the number of sensors.

We expect the relation between output and strain, $\boldsymbol{\epsilon}$, to be given by a simple diagonal gain matrix, $\mathbf{G} \in \Re^{n_s \times n_s}$

$$\boldsymbol{\epsilon} = \mathbf{GD}. \qquad (3)$$

Note that $\boldsymbol{\epsilon}$ is now a matrix. If the modeled strains are given by $\hat{\boldsymbol{\epsilon}}$,

$$\hat{\boldsymbol{\epsilon}} = \mathbf{EP}, \qquad (4)$$

then we wish to minimize, for each sensor element i,

$$\sum_j (\epsilon_{ij} - \hat{\epsilon}_{ij})^2 \quad = \quad \sum_j \left(G_{ii} D_{ij} - \sum_k (E_{ik} P_{kj}) \right)^2 .$$

3.1 Model fitted E

In the case of the model-fitted map, $\mathbf{E}$ is a nonlinear function of the sensor location, θ_{s_j}, radius, r_s, and Poisson's ratio, σ. For each sensor element, the nonlinear Simplex method [14] was used to minimize the squared strain error over these parameters. Figure 9 shows an example of one set of fitted data.

Table 1 gives summary statistics of the parameter fits over 14 sensor elements. The noise level is given for unaveraged data in units of % peak strain, and varies depending on the gain of each element. In comparing the noise level and the fitting error we must include

Parameter	Min	Avg	Max
σ	0.41	0.46	0.48
r_s (mm)	9.8	10.3	10.7
Error (% Peak)	1.28	2.16	3.95
Noise Level (% Peak)	0.95	1.72	2.87

Table 1: *Model based* **E** *fitting results. Minimum, average, and maximum values are over the 16 elements of the circumferential array.*

the noise from both the tactile sensor and the force sensor. The force sensor has a noise level equivalent to 0.5 % peak strain. The averaged tactile sensor data, which is independent of the force data, has a standard deviation of 0.4 % peak strain so we expect a fitting error of 0.9 % peak strain. Comparing this with the errors in Table 1, we see that in the best case this limit is nearly achieved while on average the error is twice the noise level indicating that model error does exist and it is on the same order of magnitude as the noise.

Calibration was also performed for both flat and edge contacts. **P** was then constructed with both the Fourier coefficients for the edge data and for Hertz contact models of the flat contact data. In accordance with the earlier discussion that predicted narrower pressure distributions in the presence of a rigid backing, it was found that the Hertz model predicted a wider strain response than was seen in the data. Use of a Hertz model resulted in an average error of 4.2 % strain while use of the frictionless contact model described in [11] resulted in an average error of 2.2 % strain. This suggests that a Hertz model can not be used to predict pressure distributions and subsurface strain on a rubber sensor with a rigid core.

3.2 Direct identification

If the sensor were constructed perfectly all the elements should have the same response, however with a manual construction method this is not always possible. Typically the model errors are most significant in the tails of the impulse response. For this reason the standard errors in the previous section were computed over a 50° range centered about the sensor. In this section we will see that direct identification of **E**, or so-called empirical calibration, does not suffer from this problem. By using direct identification of **E** one only assumes that the map from surface pressure to subsurface strain obeys linearity and superposition. It need not obey a linear elastostatic model which assumes a homogeneous and isotropic medium.

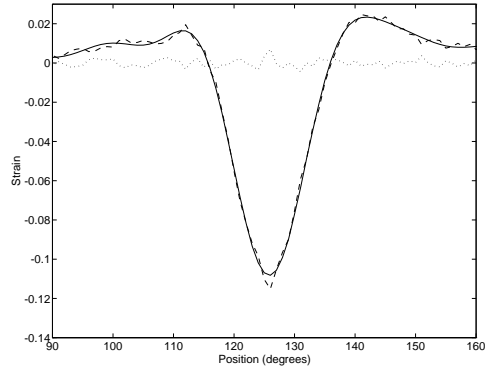Contact models are still used to generate the pres-

Figure 10: *Empirical calibration results for the third sensor element. Solid line is empirical fit, dashed is experimental, dotted is error*

Min	Avg	Max
0.93	1.41	1.76

Table 2: *Standard errors as a % of peak strain for empirical fits to edge contacts.*

sure distribution matrix, **P**, but **E** is treated as an unknown matrix that must be determined by solving for it in the equation

$$\mathbf{EP} = \mathbf{GD}. \tag{5}$$

Using standard techniques from linear least squares [19], the map **E** can be determined if **P** is full rank. For **P** to be full rank $2n_c + 1$ impulses must be applied at equally spaced intervals all the way around the finger.

E is determined directly from

$$\mathbf{E}^T = (\mathbf{PP}^T)^+ \mathbf{PD}^T \mathbf{G}^T. \tag{6}$$

The empirically derived **E** is much better at predicting the tails of the sensor as can be seen by comparing Figures 10 and 9. The average error, now computed over touches over the full 180°, is now 1.41 % of the peak strain, significantly less than the 2.16 % for the model-based fit.

The disadvantage of the identification technique is that there are no fitted parameters which can be related to the physical parameters of the sensor. One way of analyzing the linear least squares **E**, is to compare its SVD to that of the model fitted **E**. Since they are both linear maps between the same spaces they should have similar characteristics. Both maps are well-conditioned. The model fitted **E** has a condition number of 2.7 and the empirical **E** has a condition number of 3.3 . As would be expected by the line
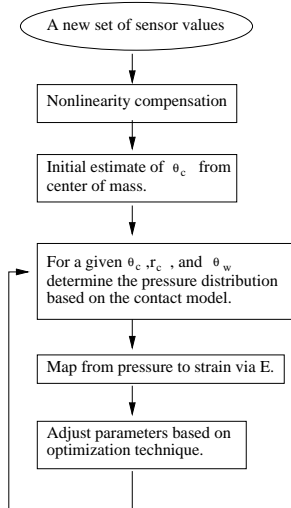
Figure 11: *Outline of the fitting procedure.*

Actual r_c	Hertz contact model		Approximate frictionless contact model	
	Model calibration	Empirical calibration	Model calibration	Empirical calibration
0.50	0.41	0.52	0.95	0.99
1.59	1.34	1.77	2.39	2.53
3.90	2.09	2.46	3.37	3.33
6.01	3.71	4.28	5.84	6.01
7.55	5.22	5.58	8.17	7.92
9.30	5.85	6.23	9.41	9.03
12.30	7.60	7.81	12.94	11.89
18.71	8.58	8.64	15.51	13.77
25.25	9.90	9.91	19.36	16.50

Table 3: *Mean r_c estimates using the Hertz and the approximate frictionless model.*

		θ_c (degrees)	P (N / m)	R (mm)
Model based	Total	0.24	13.1	1.26
	Location	0.20	9.1	1.00
	Noise	0.14	9.6	0.79
Empirical based	Total	0.24	11.7	0.96
	Location	0.19	6.4	0.60
	Noise	0.14	9.8	0.77

Table 4: *Standard deviation of errors in parameters fitted for 40 touches at 1 degree intervals of 6 different indenter radii ranging from edge to flat contact.*

load frequency response, the well conditioned directions in **V** column space, pressure Fourier coefficients, have most of their energy in the center of the theoretical frequency response. The more poorly conditioned directions have their energy concentrated in the very low and high frequencies [10].

4 Shape from strain

In Figure 5 the relationship between the various maps and contact models is shown with the forward directions going from left to right. It is clear that if we use a Hertz model there is an easy forward path from contact parameters to sensor values. Using the Simplex algorithm and **E**, contact parameters were fitted to the sensor data, as is shown in Figure 11. The typical execution time of 0.1 second on a Sparc 20 could be reduced to 0.04 second when total load information from a force sensor was used. In the discussion of the parameter fits to experimental data we will investigate three different phenomena that affect the indenter radius estimation errors: noise, the **E** matrix, and the contact model.

As might have been predicted by the fitting results in Section 3.1, it was found that use of a Hertz contact model to predict subsurface strains resulted in a biased estimate of the indenter radius. Table 3 gives the mean estimate of r_c over 40 degrees for 9 different indenters. Concentrating for now on the results for the Hertz model, it was found that r_c was consistently underestimated when using both the empirical and model-based calibration. Since the other contact model that has been discussed, the frictionless contact model, requires the inversion of a large matrix to de-

termine the pressure distribution, it was approximated by squeezing and stretching a Hertz model. We call this new contact model the "approximate frictionless contact model." In Table 3, we see that this model is much better at giving an unbiased estimate of r_c for indenters of radius 13 mm and less. All the results in the following sections were obtained using the approximate frictionless contact model.

If the only source of variance in the data were random, uncorrelated, and stationary noise and time response were not a consideration then estimation errors could be reduced by averaging the data over an adequate number of samples. Unfortunately we will see that the parameter estimate depends, in a consistent manner, on where the probe touches the sensor.

This effect became apparent when comparing summary statistics for averaged and raw data. Table 4 gives the standard deviations of the errors in the fitted contact parameters. The rows labeled "Total" are the standard deviations computed over 20 samples each of 40 touches using 6 different indenter radii. The rows labeled "Location" are the standard deviations of the errors in parameters fitted to 20 times averaged data. These rows indicate the variance due to location. The rows labeled "Noise" are the standard deviations of the errors in parameters fitted to raw data after
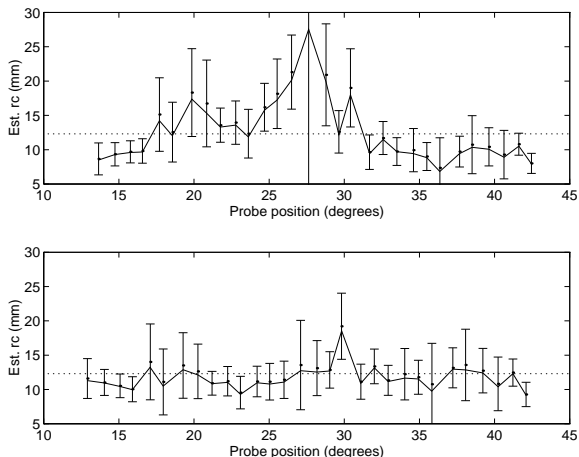
Figure 12: *Estimates of r_c for a 12.3 mm radius indenter. The top plot uses a model based **E** while the bottom plot uses an empirical **E**. In both cases the dotted line is the actual r_c, the solid line is the fitted r_c to 20 times averaged data, and the error bars indicate the mean plus and minus one standard deviation for fits to the raw data.*

subtraction of the estimate to the averaged data at each location. These rows indicate the variance due to noise.

Contact location estimation error is very small, $\frac{1}{25}$th of the sensor spacing. If we include only the sensor noise than the standard deviation is halved. As might be expected from our frequency domain and SVD analysis of **E**, total load estimates are noisy, with a standard deviation of 5 % of the applied load.

Table 4 gives the standard deviation of the radius estimate in terms of R. This is necessary when discussing flat contacts since one would expect the standard deviation of r_c in that case to be infinite. For small radius contacts the standard deviation in R and r_c will be approximately the same. For $r_c = r_b$ the standard deviation in r_c will be twice that for R. The standard deviation in R due to noise is 0.77 mm, meaning that for small r_c indenters, radii differences of 1.5 mm should be distinguishable at a 95 % level at a fixed location. Figure 12 shows estimates for r_c for averaged and raw data. We see that the standard deviation of the estimate at a particular location is often less than the bias due to location. It is also apparent that the standard deviation due to noise also depends on location. In other words, in addition to the systematic bias, some locations provide more consistent estimates than other locations.
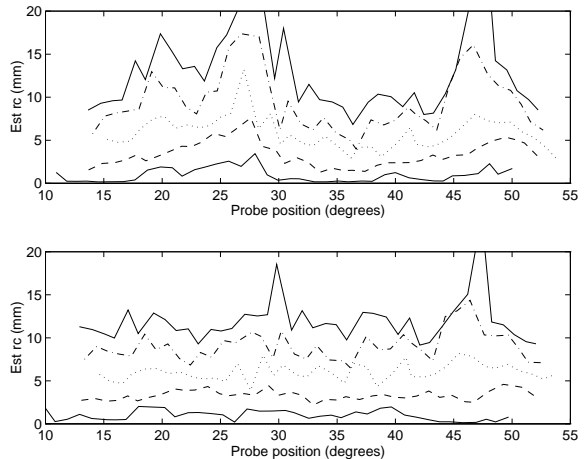
It is interesting to see that the location dependent

Figure 13: *Estimate of r_c using model-based (top) and empirical (bottom) calibration on 20 times averaged data. From lower to upper trace $r_c = \{0.5, 3.90, 6.01, 9.30, 12.30\}$mm.*

bias in the estimate of r_c is consistent across indenters. Figure 13 shows r_c estimates for 5 different indenters as a function of location. For both calibrations the estimate of r_c is monotonic at each location, although the bias might be considerable. This indicates that the information about curvature is contained in the data, however the model used to estimate curvature is not quite correct.

5 Conclusions

This paper has discussed the ability of linear elastic models and general linear models to predict subsurface strains in a tactile sensor. There are two linear elastic models of concern here, one is a linear map from surface pressure to subsurface strain, the **E** map, the other is a nonlinear map from indenter shape to surface pressure, **S**. We have seen that **E** can predict strains to a precision commensurate with signal noise for a well constructed sensor; however if there are inhomogeneous artifacts in the sensor response due to construction, the linear least squares approach will produce a better result. One may conclude that a sensor can be constructed that will result in an impulse response like that predicted by a linear elastic model. However, when it comes to using a hand-made sensor, it is apparent that an empirical technique can provide a more consistent prediction of sensor responses.

The parameter fitting results showed that contact location can be estimated to a precision of $\frac{1}{25}$th of the sensor spacing. Estimates of R and r_c were seen to be sensitive to the calibration technique. Results using the model based calibration indicate that cur-

vature estimation at a fixed location could be reliable and monotonic, however each location showed a bias. Using 20 times averaging and the empirical calibration R could be estimated with a standard deviation of 0.60 mm.

Calibration of tactile sensors via $\mathbf{E}$ allows retention of linear elastic theory for contact models, which are well understood, but allows compensation for some of the characteristics of the sensor response that are not predicted by linear elastic theory. There is room for improvement in techniques for the estimation of $\mathbf{E}$, however we leave investigation of other more probabilistic approaches as future work. It would be interesting to see if a general nonlinear map approximator, such as a neural net, could compensate for the inhomogenous, anisotropic, and nonlinear qualities of an actual sensor. Alternatively there is a lot of room for improvement in the construction methods which might allow more uniform and linear sensor responses.

Acknowledgements

References

[1] R. A. Boie. Capacitance impedance readout tactile image sensor. In *Proceedings, IEEE International Conference on Robotics and Automation*, pages 370–378, Atlanta, Georgia, Mar. 1984.

[2] G. Canepa, M. Morabito, D. De Rossi, A. Caiti, and T. Parisini. Shape from touch by a neural net. In *Proceedings, IEEE International Conference on Robotics and Automation*, pages 2075–2080, Nice, France, May 1992.

[3] R. E. Ellis and M. Qin. Singular-value and finite-element analysis of tactile shape recognition. In *Proceedings, IEEE International Conference on Robotics and Automation*, pages 2529–2535, San Diego, CA, May 1994.

[4] R. S. Fearing. Tactile sensing mechanisms. *The International Journal of Robotics Research*, 9(3):3–23, June 1990.

[5] R. S. Fearing and T. O. Binford. Using a cylindrical tactile sensor for determining curvature. *IEEE Transactions on Robotics and Automation*, 7(6):806–817, Dec. 1991.

[6] A. W. Goodwin, K. T. John, and A. H. Marceglia. Tactile discrimination of curvature by humans using only cutaneous information from the fingerpads. *Experimental Brain Research*, 86(3):663–672, 1991.

[7] B. L. Hutchings, A. R. Grahn, and R. J. Petersen. Multiple-layer cross-field ultrasonic tactile sensor. In *Proceedings, IEEE International Conference on Robotics and Automation*, pages 2522–2528, San Diego, CA, May 1994.

[8] K. L. Johnson. *Contact Mechanics*. Cambridge University Press, Cambridge, England, 1985.

[9] H. Maekawa, K. Tanie, K. Komoriya, M. Kaneko, C. Horiguchi, and T. Sugawara. Development of a finger-shaped tactile sensor and its evaluation by active touch. In *Proceedings, IEEE International Conference on Robotics and Automation*, pages 1327–1334, Nice, France, May 1992.

[10] E. J. Nicolson. *Tactile Sensing and Control of a Planar Manipulator*. PhD thesis, University of California at Berkeley, Nov. 1994.

[11] E. J. Nicolson and R. S. Fearing. Sensing capabilities of linear elastic cylindrical fingers. In *IEEE/RSJ International Conference on Intelligent Robots and Systems*, pages 178–185, Yokohama, Japan, July 1993.

[12] D. Nowell and D. A. Hills. Tractive rolling of tyred cylinders. *International Journal of Mechanical Sciences*, 30(12):945–957, 1988.

[13] F. Oberhettinger. *Fourier transforms of distributions and their inverses; a collection of tables*. Springer-Verlag, New York, 1990.

[14] W. H. Press, S. A. Teukolsky, W. T. Vetterling, and B. P. Flannery. *Numerical Recipes in C : The Art of Scientific Computing*. Cambridge University Press, New York, 2nd edition, 1992.

[15] D. Reynaerts and H. V. Brussel. Tactile sensing data interpretation for object manipulation. In *Sensors and Acutators A*, pages 268–273, June 1993.

[16] M. Shimojo. Spatial filtering chracteristic of elastic cover for tactile sensor. In *Proceedings, IEEE International Conference on Robotics and Automation*, pages 287–292, San Diego, CA, May 1994.

[17] D. M. Siegel, S. M. Drucker, and I. Garabieta. Performance analysis of a tactile sensor. In *Proceedings, IEEE International Conference on Robotics and Automation*, pages 1493–1499, Raleigh, NC, Mar. 1987.

[18] T. H. Speeter. Flexible, piezoresistive touch sensing array. In *SPIE - The International Society for Optical Engineering*, volume 1005, pages 31–43, Nov. 1988.

[19] S. Van Huffel and J. Vandewalle. *The Total Least Squares Problem : Computational Aspects and Analysis*. Society for Industrial and Applied Mathematics, Philadelphia, 1991.

A   The Hertz contact

Under the assumption of frictionless contact between a cylinder and an elastic half space the Hertz model predicts an elliptical pressure distribution. (See [8] page 129 and following.) For the contact of a rigid cylinder and and elastic cylinder, the equivalent radius, R, may be used. It should be noted that the Hertz assumption is no longer valid for cylinders with a rigid core [12], however when the contact area is small and the elastic layer is thick the approximation is sufficient.

The elliptic pressure distribution is given by

$$p(\theta) = \frac{\mu}{1-\sigma}\left(1+\frac{r_b}{r_c}\right)\left(\left(\frac{\theta_w}{2}\right)^2 - \theta^2\right)^{\frac{1}{2}} \qquad (7)$$

where the arc of contact, in radians, θ_w, is given by

$$\theta_w = \frac{2}{r_b}\sqrt{\frac{2P(1-\sigma)}{\pi\mu}\left(\frac{1}{r_b}+\frac{1}{r_c}\right)} \qquad (8)$$

and P is the load in N/m.

We can find the fourier series coefficients for the Hertz contact at θ_c from a standard table [13]

$$
\begin{aligned}
p_0 &= \frac{\mu}{4(1-\sigma)}\left(1+\frac{r_b}{r_c}\right)\left(\frac{\theta_w}{2}\right)^2 \\
p_k^s &= \frac{\mu}{2(1-\sigma)}\left(1+\frac{r_b}{r_c}\right)\left(\frac{\theta_w}{k}\right)J_1\left(\frac{\theta_w}{2}k\right)\sin(k\theta_c) \\
p_k^c &= \frac{\mu}{2(1-\sigma)}\left(1+\frac{r_b}{r_c}\right)\left(\frac{\theta_w}{k}\right)J_1\left(\frac{\theta_w}{2}k\right)\cos(k\theta_c). \quad (9)
\end{aligned}
$$

where J_1 is the Bessel function of the first kind.